THE ASTROPHYSICAL JOURNAL, 420:746–755, 1994 January 10

FABRY-PEROT IMAGING OF MOLECULAR HYDROGEN EMISSION IN ORION-KL REGION

HAJIME SUGAI, TOMONORI USUDA, HIROKAZU KATAZA, AND MASUO TANAKA
Institute of Astronomy, University of Tokyo, Mitaka, Tokyo 181, Japan
MOTOKO Y. INOUE
Department of Physics, Waseda University, Shinjuku-ku, Tokyo 169, Japan
HIRONOBU KAWABATA
Tokyo Gakugei University, Koganei, Tokyo 184, Japan
AND
HIDEKI TAKAMI, TETSUO AOKI, AND NORIHISA HIROMOTO
Communications Research Laboratory, Koganei, Tokyo 184, Japan
Received 1993 April 5; accepted 1993 July 19

ABSTRACT

A continuum-subtracted image of the H_2 $v = 1–0$ $S(1)$ line covering the central 4′ square portion of the Orion-KL region, has been obtained using a wide-field Fabry-Perot imager at the Communications Research Laboratory 1.5 m telescope. Nine H_2 peaks (including four newly identified) are found in the core, as well as a curved, bridgelike structure that encroaches on the inner edge of the disk structure observed in CS ($J = 1–0$) emission. This existence of the bridge indicates that the outflow from IRc2 occurs not only toward the bipolar axis but also toward the disk, and suggests channeling by the disk of a more or less isotropic flow from IRc2 into a bipolar flow. Outside the core, where finger-like features of H_2 emission are seen, we identify 43 hot H_2 clumps. These are located along filamentary structures seen in CS ($J = 1–0$) maps and avoid peaks of CS intensity. The geometrical thickness of the hot H_2 in these features is much smaller than their typical dimensions. We conclude that the H_2 emission from the clumps is radiated at the surfaces of the CS filaments, implying that outflow from IRc2 shocks the H_2 at the surfaces. From comparison of polarization measurements of Burton et al. (1991) with the present measurements, as well as from discussion of the energetics, we rule out the possibility that the H_2 clumps are due to reflection.

Subject headings: ISM: individual (Orion Nebula) — ISM: jets and outflows — ISM: molecules — shock waves

1. INTRODUCTION

The recent development of infrared array detectors has made it possible to obtain infrared-line images with high spatial resolution. Infrared molecular hydrogen emission lines in vibrational transitions have been detected toward objects such as bipolar flows, planetary nebula, and supernova remnants. The spectroscopic characteristics of these lines indicate the existence of shock phenomena. In the case of bipolar flows, high spatial resolution H_2 line images provide us insight into the key phenomena in the star formation process, i.e., the outflow mechanism and the interaction between the flow and the ambient cloud.

In order to obtain pure line emission image for a better understanding of such key phenomena, the contamination by the continuum has to be eliminated. The $H_2 = 1–0$ $S(1)$ images of bipolar flow sources, Cepheus A, Orion-KL (Lane 1989), DR 21, and NGC 2071 (Garden, Russell, & Burton 1990), have been obtained by using a narrow-band filter. However, the spectral resolution of a narrow-band filter was not high enough to remove contamination by the continuum. The contamination made it difficult to investigate the collimation mechanism around the sources—in particular, in regions close to the central sources where reflected and thermal continuum radiation is strong.

In addition to an accurate continuum subtraction, a large field of view is needed in order to discuss bipolar flow phenomena systematically: the collimation of the flow around the central source and the interaction between the flow and the ambient cloud. Continuum-subtracted H_2 images have been obtained for bipolar flow sources, S106 (Hayashi et al. 1990) and NGC 2071 (Aspin, Sandell, & Walther 1992), using a Fabry-Perot imager with a field of view, 0.′6 × 0.′6. The image of NGC 2071 covered only a part of the bipolar structure, so that discussion concentrated on the central region. The image of S106 with a 1′ × 1′ area was obtained by registering five frames. However, registering frames in general degrades the quality of images due to the variations of seeing, atmospheric transmission, and background emission among frames, and also degrades the positional accuracy.

We obtained the continuum-subtracted H_2 $v = 1–0$ $S(1)$ images of the Orion-KL region, using a Fabry-Perot imager we have developed. Its large field of view, 4.′0 × 4.′0, allows us to take the whole shocked H_2 region in a single frame. The Orion-KL region has the best-studied bipolar flow, which enables us to compare our data with those in other wavelengths in detail.

2. OBSERVATIONS

The H_2 $v = 1–0$ $S(1)$ image was obtained using the Communications Research Laboratory (CRL) 1.5 m telescope at Tokyo, which was equipped with a near-infrared Fabry-Perot imager on its Nasmyth focus (Sugai et al. 1994). A K-band etalon with 85 min effective aperture made by Queensgate Instruments was set in a collimated beam. A cooled narrow-band filter (1%) was used for sorting an order of interference. A near-infrared camera used here houses a Rockwell HgCdTe

TABLE 1

CONFIGURATION OF THE FABRY-PEROT IMAGER

Parameter	Value
Telescope: Communications Research Laboratory 1.5 m	
Nasmyth F-ratio	17.5
Detector: Rockwell HgCdTe (1–2.5 μm), 128 × 128 pixel	
Pixel size	60 μm spacing = 1.″88
Quantum efficiency	20% at K band[a]
Readout noise	700e^- rms[b]
Gain	340e^-/DN
Field of view	4.′0 × 4.′0
Fabry-Perot Etalon: Queensgate Instruments ET85	
Etalon effective area	85 mm
Etalon spacing	~27.2–29.1 μm[c]
Effective finesse	~45
Order	~26
Velocity resolution	~250 km s^{-1}
Parallelism of etalon	5 nm
Accuracy of wavelength calibration	~10% of velocity resolution for J band; ~7% of velocity resolution for K band
Focal length of collimator	470 mm

[a] Including the transmission of a Dewar window and camera lenses.

[b] A net mode, which needs two frames, is used for correcting the time variation of the offset. Therefore, the readout noise for a resultant frame is $\sqrt{2}$ times this value.

[c] The range depends on a controller and its setting within the shift of ~1 μm.

array of 128 × 128 pixels with 60 μm spacing and has a field of view of 4.′0 × 4.′0. The Fabry-Perot system includes a He-Ne laser for realizing an accurate parallelism of an etalon and also a Kr lamp for wavelength calibration. The spectral resolution is 250 km s^{-1}. The integration time was 10 minutes for each of two on-line frames and two off-line frames. The total spatial resolution, including the seeing, the tracking error, and the effect from adding and subtracting those four frames, was 5.″3 (FWHM). The configuration of our Fabry-Perot imager and the summary of the observations are given in Tables 1 and 2, respectively.

3. DATA REDUCTION

The data reduction was done using IRAF[1] and also the programs that we have developed for the Fabry-Perot imaging. At first the nonlinearity of the sensitivity of the camera was corrected (the quantum efficiency $\eta \propto I^{\alpha}$, where I is the obtained signal and $\alpha \simeq 0.07416 \pm 0.00127$). Next, flat-fielding was carried out using K-band sky frames. Flux calibration was done through the photometry of θ^1C, the brightest star in the Trapezium at the K-band (O6; 4.36 mag at 2.2 μm [Lee 1968]; its spectrum is assumed to follow the Rayleigh-Jeans law). After the application of the flux calibration for each frame, two on-line ($v = v_{LSR} = 0$ and $+100$ km s^{-1}; see below) frames were added, and two off-line ($v = \pm 510$ km s^{-1}; continuum) frames were subtracted from the added frame in order to obtain a continuum-subtracted line image. From this image, we subtracted a constant, about two orders of magnitude less than the peak intensity, in order to set the output signal at ~0 in the outer region of the frame. It was impossible to discuss the subtacted constant as a diffuse H_2 component. This is because it was difficult to determine a sky level, owing to the large extent of the diffuse component (Burton & Puxley 1990) and also because the time variation of the background was relatively large.

In observations using a Fabry-Perot imager, the wavelength of the peak transmission varies over the field of view. We call this variation "velocity shift" or "phase shift." For our instrument, this velocity shift is expressed as Δv (km s^{-1}) $= -35\theta^2$ (arcmin^2), where Δv is the wavelength difference in terms of velocity and θ is the angular distance from the velocity center, which was set at the position of IRc2. The shift at the edge of the frame is -140 km s^{-1}, which is smaller than the spectral resolution (250 km s^{-1}). Therefore, it is possible to obtain a line image with roughly a uniform transmission for the H_2 emission over the frame by carrying out only a few scanning steps and adding the obtained frames if the spatial variation of the peak velocity of the line from an object and its line width are small enough. We have obtained two on-line frames, which are optimized for velocities of $v = 0$ and $+100$ km s^{-1} at the position of IRc2. In other words, the frame with $v = 0$ km s^{-1} was optimized so that the maximum transmission for the H_2 line is at the position of IRc2, while the frame with $v = +100$ km s^{-1} was optimized at points 1.′7 away from IRc2. When we add these two frames, the transmission for the H_2 line is uniform within ±4% over almost the whole frame (within 1.′6 from IRc2). We have carried out a correction for this small variation in order to obtain a completely flux-corrected line image. According to Scoville et al. (1982), the peak velocities, v_{LSR}, for the H_2 line at 12 positions range only from -19 to $+11$ km s^{-1}. Therefore, the assumption that the spatial variation of the peak velocity is small enough compared with the spectral resolution ($\delta v = 250$ km s^{-1}) is valid at least for the region observed by Scoville et al. (1982). The line width in the Orion-KL region, ~50 km s^{-1} (FWHM; see Fig. 7 of Scoville et al. 1982; also see Nadeau & Geballe 1979), was also found to be so small that the spatial variation and uncertainty of the line profile do not affect the correction. Although we make a correction for a variation of transmission when we discuss H_2 line flux (Tables 3 and 4), we show figures without a correction. This is because the variation is small over a wide range and also because we want to show figures with a common noise level over the whole frame.

The equatorial coordinate was determined by using the positions of BN [$\alpha(1950.0) = 5^h32^m46^s.64 \pm 0^s.01$, $\delta(1950.0) =$

TABLE 2

SUMMARY OF THE OBSERVATIONS

Parameter	Value
Date	1992 Jan 12
Line	H_2 $v = 1$–0 $S(1)$:2.122 μm
Velocity resolution	250 km s^{-1} [a]
Center velocity	0, +100, ±510 km s^{-1} [b]
Exposure time	10 minutes[c]
Spatial resolution	5.″3[d]

[a] The uncertainty is a few percent.

[b] At the position of IRc2 for each frame. The uncertainties for the velocities are within ±10 km s^{-1}.

[c] For each frame.

[d] For the final frame, which was made from four frames (see text).

[1] IRAF is distributed by the National Optical Astronomy Observatories, which are operated by the Association of Universities for Research in Astronomy, Inc. (AURA), under cooperative agreement with the National Science Foundation.

$-5°24'16''.45 \pm 0''.1$: Moran et al. 1983] and θ^1 Ori C [$\alpha(1950.0) = 5^h32^m49^s.03$, $\delta(1950.0) = -5°25'16''.7$: cf. Khrutskaya 1984]. Based on these two positions, we have checked the position of a pointlike bright continuum source located far from both BN and θ^1 Ori C to find that its position and K-magnitude are consistent with those obtained by Hyland et al. (1984; $\alpha(1950.0) = 5^h32^m47^s.19 \pm 0^s.03$, $\delta(1950.0) = -5°22'34''.5 \pm 0''.3$, 8.8 mag at 2.2 μm). Therefore, we conclude that the error of the defined coordinate is less than 1″ over the whole frame.

4. AN OVERVIEW OF THE H_2 EMISSION REGION

Figure 1 shows the continuum-subtracted emission-line image of H_2 $v = 1$–0 $S(1)$ for the Orion-KL region, with its contour map. We confirm five peaks (peaks 1–5) found by Beckwith et al. (1978), who have mapped a smaller extent of the BN-KL region. Moreover, within the region where the line intensity is larger than 5.7×10^{-21} W cm^{-2} arcsec^{-2}, we define two peaks (peaks 6 and 8) which cannot be recognized in their map and also two peaks (peaks 7 and 9) which are outside their mapped region. We can confirm the presence of these four peaks also in Figure 1 of Burton et al. (1991), although their figure was made in a mosaic configuration and included continuum emission. The finger-like features, including many small clumps of the H_2 emission as described in § 6, are clearly seen outside the region mapped by Beckwith et al. (1978). For further discussion, we separate our H_2 image into two parts: the part where the H_2 line intensity is larger than 5.7×10^{-21} W cm^{-2} arcsec^{-2} (the central region) and the part with the H_2 intensity smaller than that (the finger region; cf. Taylor et al. 1984). The mapped region by Beckwith et al. (1978) roughly corresponds to the central region.

The column density of hot H_2 molecules, N_{H_2} (cm^{-2}) is estimated by using the following equation:

$$I_{S(1)} = 2.35 \times 10^{-11} \frac{N_{H_2} f_{v=1,J=3} A_{S(1)} h\nu}{4\pi D^2}, \quad (1)$$

where $I_{S(1)}$(W cm^{-2} arcsec^{-2}) is the observed H_2 $v = 1$–0 $S(1)$ line intensity. The population fraction in the $v = 1$, $J = 3$ level, $f_{v=1,J=3}$, is 1.22×10^{-2} for $n_{H_2} > 10^{4.5}$ cm^{-3} and $T_{vib} = 2000$ K (Scoville et al. 1982), and the transition probability $A_{S(1)}$ is 3.47×10^{-7} s^{-1} (Turner, Kirby-Docken, & Dalgarno 1977). The energy per photon, $h\nu$, is 9.35×10^{-20} J and the distance D to Orion-KL is 450 pc (e.g., Genzel & Stutzki 1989). As a result, we obtain the following equation:

$$N_{H_2}(\text{cm}^{-2}) = 1.35 \times 10^{39} I_{S(1)} \text{ W cm}^{-2} \text{ arcsec}^{-2}. \quad (2)$$

The hot H_2 column density, e.g., 2.8×10^{19} molecules cm^{-2} at peak 1, is much smaller than 10^{26} molecules cm^{-2}, which corresponds to the optical thickness of unity for H_2 $v = 1$–0 $S(1)$ (Beckwith et al. 1978). Therefore, the H_2 emission is optically thin.

5. THE CENTRAL REGION

5.1. *Positions and Intensities of* H_2 *Emission Peaks*

Table 3 gives the positions and intensities of nine H_2 peaks in the central region. The positions of peaks 1–5, except for the right ascension of peak 3 and the declination of peak 1 (4″–5″ differences), are consistent within $\pm 2''.4$ with those obtained by Beckwith et al. (1978). According to them, their positional accuracy was probably better than $\pm 2''$. The H_2 line intensities at peaks 1–5 are also consistent with those obtained by Beckwith et al. (1978) within the errors. The other four peaks were newly found in *continuum-subtracted* images.

TABLE 3

POSITIONS AND INTENSITIES OF H_2 EMISSION PEAKS IN THE CENTRAL REGION

Peak	Position[a] α(1950.0) $5^h32^m +$	Position[a] δ(1950.0) $-5° +$	Intensity ($\times 10^{-20}$ W cm^{-2} arcsec^{-2}) This Work[b] 5″.6 × 5″.6	This Work[b] (10″.0 diameter)	Beckwith et al.[c] 10″.0 diameter	Corresponding Features from Molecular Observations
1	46^s.09	23′57″.3	2.09	(1.87)	1.76	CS (1–0) ridge F[d]
2	48.27	24 33.3	1.45	(1.32)	1.18	CS (1–0) ridge H[d]
3	47.58	24 27.6	0.93	(0.83)	0.78	CS (2–1) hot core[d]
4	46.32	24 25.3	0.84	(0.76)	0.75	CS (2–1) hot core[d]
5	46.38	23 47.6	1.75	...	[e]	...
6	45.83	24 12.8	1.45	...	...	CS (1–0) and NH_3 (1, 1) ridge[d,f]
7	46.80	23 46.2	1.28	...	...	...
8	46.69	24 30.8	0.81	...	...	CS (2–1) hot core[d]
9	45.46	24 41.7	0.57	...	...	CS (1–0) ridge[d]

[a] The uncertainties mainly originate from the pixel scale (1″.88 pixel^{-1}). A simple simulation using artificial data with noise has shown that the uncertainties are less than $\pm 1''$, not including the systematic error of the coordinate itself.

[b] The intensities were obtained by averaging those within 3 × 3 pixels (5″.6 × 5″.6) and also within a diameter of 10″.0 of four peaks for the comparison with the results obtained by Beckwith et al. 1978. The variation of the transmission over the frame was corrected assuming that the spatial variation of the peak velocity in Orion-KL was small enough compared with the instrumental resolution and also that the line width in Orion-KL was ~50 km s^{-1} (FWHM). The uncertainties of the intensities mainly originate from the uncertainties of the scanned velocities, the spectral resolution, and the assumption of the line width in Orion-KL and also from the uncertainties of the estimate of the line contamination into the continuum frame. Also taking a readout noise into consideration, we conclude that the uncertainties are less than $\pm 10\%$. Note that the correction for extinction is not carried out. If it is carried out using the *average* extinction value for the central 17″ × 17″ region, $A_{2.1\mu m} = 2.1$ mag (Davis et al. 1982), these values have to be multiplied by 6.9.

[c] The intensities obtained by Beckwith et al. 1978 with a 10″ aperture. Uncertainties are $\pm 10\%$. The correction for extinction is not carried out.

[d] Murata 1991.

[e] Although Table 1 of Beckwith et al. 1978 does not show the intensity for peak 5, their contour map with 5″ resolution (Fig. 2) shows that the intensity for peak 5 is between those for peaks 1 and 2.

[f] Murata et al. 1989.

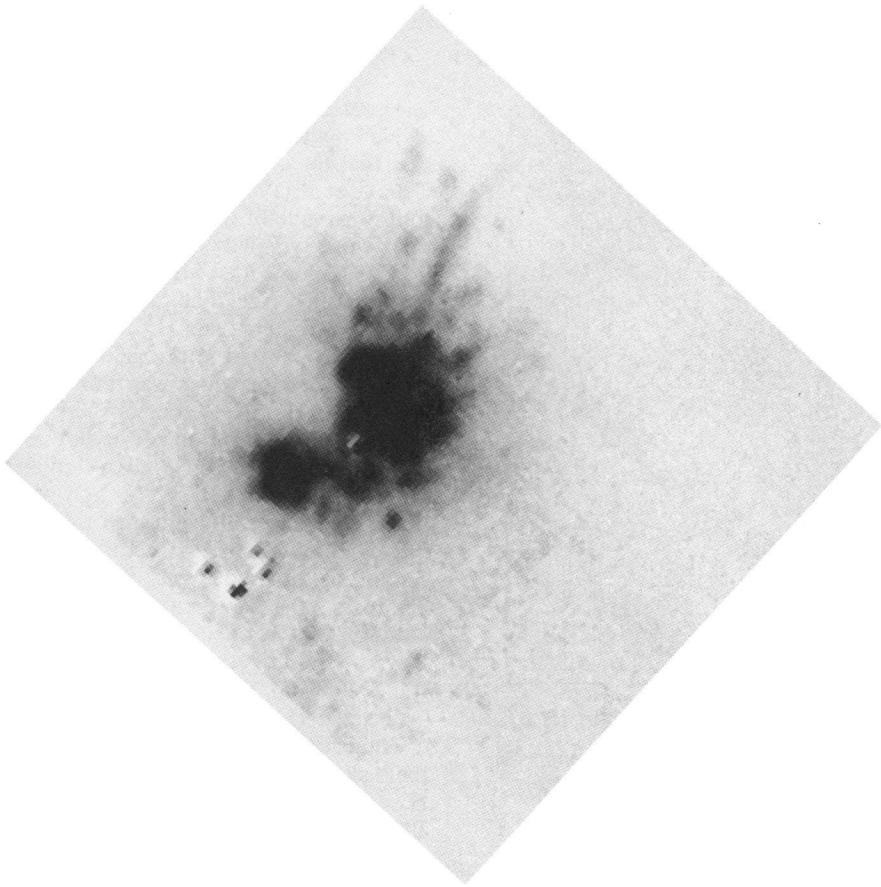

FIG. 1*a*

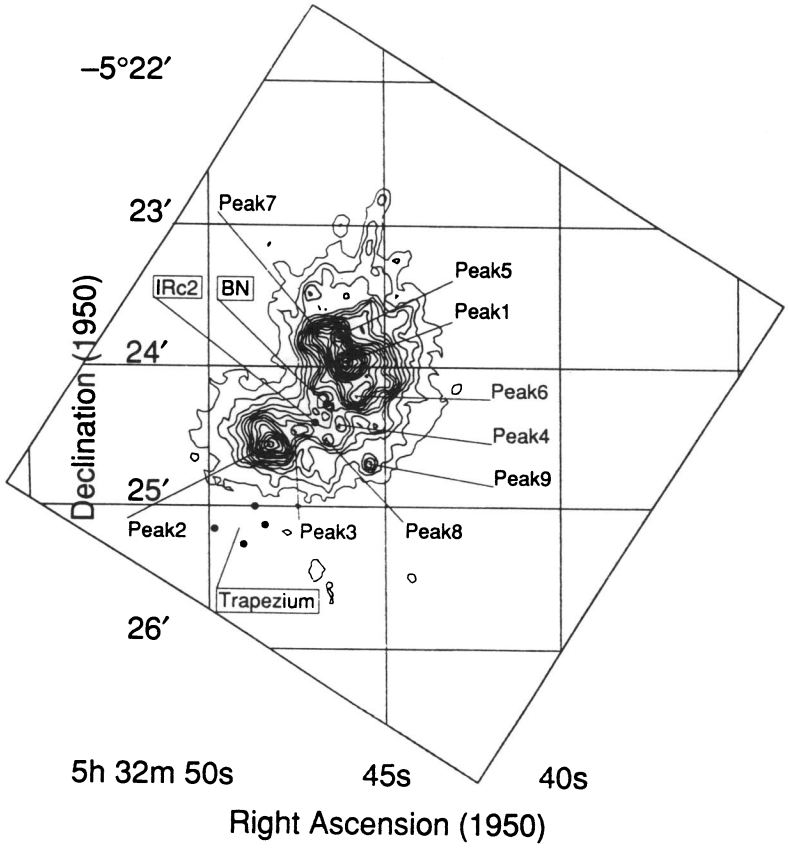

FIG. 1*b*

FIG. 1.—(*a*) Continuum-subtracted line image of H_2 $v = 1$–0 $S(1)$ for Orion-KL region. Because of many bad pixels, we replaced the lowest ~10 pixel width of the frame by the value zero. (*b*) Contour map of the continuum-subtracted image. The contour intervals are 8.2×10^{-22} W cm^{-2} arcsec^{-2} with the lowest contour level 2.5×10^{-21} W cm^{-2} arcsec^{-2}. The variation of the transmission over the frame is small (±4% within 1.′6 from IRc2; see text) and has not been corrected in this figure because we want to show the figure with a common noise level over the whole frame.

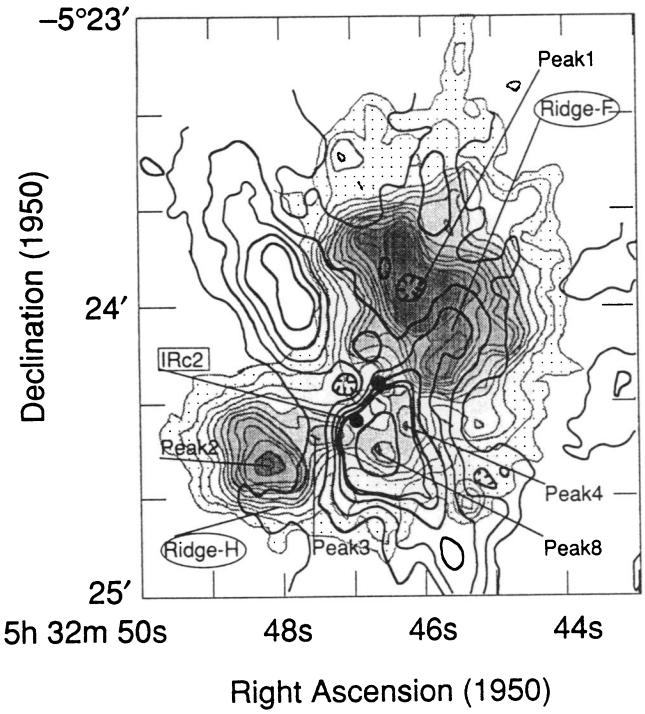

FIG. 2.—H_2 image (*gray*) superposed on the CS (1–0) map obtained by Murata (1991). The bridgelike structure in the H_2 emission includes peaks 3, 4, and 8. The contour levels for the CS (1–0) map are 3.35, 10.05, 16.75, 23.45, 30.15, 33.5, 67.0, and 100.5 K km s^{-1}.

5.2. *Outflow toward the Disk*

In Figure 2 the H_2 image is superposed on the molecular CS (1–0) map obtained by Murata (1991; 8.″0 × 5.″6 FWHM with the position angle of 3.°0). The H_2 emission extends from IRc2 to the northwest and to the southeast. This is roughly perpendicular to the disk structure of CS (1–0), which is elongated from the northeast to the southwest. The central source, IRc2, is largely affected by extinction, and its bolometric luminosity is estimated to be $\sim 10^5\ L_\odot$ when it is corrected for extinction (Downes et al. 1981; Wynn-Williams et al. 1984).

It is remarkable that a curved bridgelike structure in the H_2 emission exists at a distance of $\sim 4 \times 10^3$ AU from IRc2, connecting peaks 1 and 2. Along the bridgelike structure, there are three peaks: peaks 3, 4, and 8. In particular, peak 8, which was newly defined in this paper, is located almost at the center of the bridgelike structure and is coincident with the CS (1–0) intensity peak of the southwest side of the disk. The bridgelike structure implies that the outflow from IRc2 compresses the inner side of the disk, forming the curved, compressed shell and also exciting shocked H_2 emission. We emphasize that at small distances from IRc2 the outflow is roughly isotropic, proceeding not only along the large-scale bipolar axis but also toward the disk. This finding gives a strong restriction to the most significant and controversial issues of bipolar outflows: the origin of outflows and their collimation mechanism. The outflow component toward the disk cannot be explained by models with an intrinsically collimated flow, which is accelerated by the twisted magnetic fields along the poles of a magnetized disk (e.g., Pudritz & Norman 1983, 1986; Uchida & Shibata 1984, 1985). The structure found in the H_2 image suggests that channeling of a more or less isotropic flow into a bipolar flow caused by the molecular disk is a more plausible interpretation, although it is not yet known how such an isotropic flow forms. This conclusion is consistent with a conclusion that the outflow has a very large opening angle, made by Geballe et al. (1986). The bridgelike structure is seen only in the southwest side of the disk, i.e., it is not seen in the northeast side. This asymmetry is probably caused by the fact that IRc2 is located closer to the inner disk in the southwest side than in the northeast side. The flow from IRc2 will excite a weaker shock to radiate weaker H_2 emission in the northeast side.

Figure 3 shows the bridgelike structure superposed on the CS (2–1) hot core, which was found to be an expanding shell by Murata (1991). The center of the bridgelike structure is coincident with the position of the hot core. The curved shape of the bridgelike structure is also similar to the curved shape of the hot core. These facts strongly support the interpretation that the H_2 emission from the bridgelike structure is related to the expanding shell structure. These structures, however, cannot be the same gas, because they have different temperatures: the temperature of the H_2 emission region is $\sim$1500–2000 K (Beckwith et al. 1978; Scoville et al. 1982; Davis, Larson, & Smith 1982), while the temperature is 100 ± 20 K at the southern peak of the CS (2–1) intensity (Murata 1991).

The bridgelike structure seen in H_2 probably is a portion of the disk in the process of being blown away. By modeling the H_2, CO, and OH infrared emission-line intensities in the BN-KL region by shock waves traveling at $v_s \simeq 36$ km s^{-1} with respect to ambient gas, Chernoff, Hollenbach, & McKee (1982) have estimated the total ejected momentum from IRc2 to be 10^{41} g cm s^{-1}, which is adequate to disrupt a gravitationally bound cloud of $200(n/10^5\ \mathrm{cm}^{-3})^{-1/8}\ M_\odot$. This is close to the mass of the disk surrounding IRc2, 190 $M_\odot$ (Murata 1991), suggesting the possibility that the ejected momentum is enough to blow away the disk to make the central source

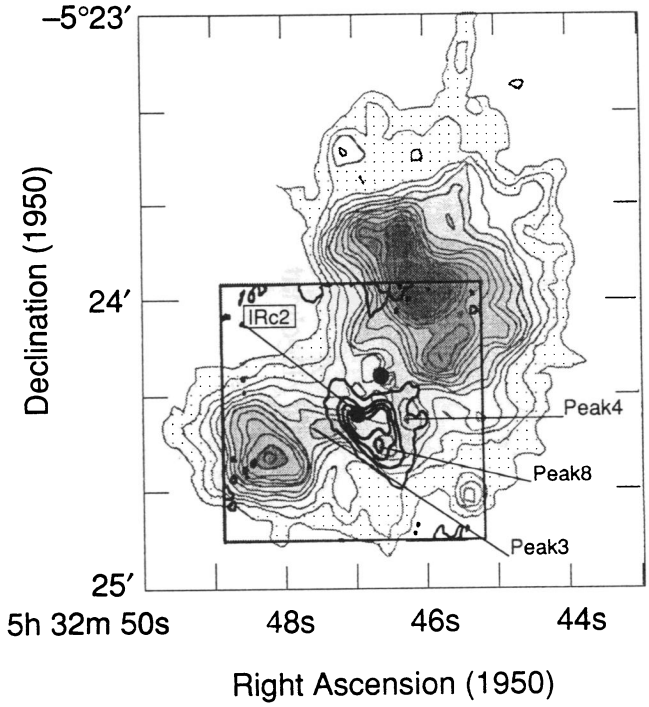

FIG. 3.—Bridgelike structure in the H_2 emission superposed on the CS (2–1) hot core, which was found to be an expanding shell by Murata (1991).

visible. The bridgelike structure is probably a place where the ejected momentum from IRc2 is transferred into the disk to blow away the disk. This idea also can be applied to the bright H_2 emission along the bipolar axis. Peaks 1 and 2 correspond to ridges F and H of CS (1–0), respectively, found by Murata et al. (1989) and Murata (1991). The morphological relation between the H_2 peaks and the extended CS (1–0) ridge structures implies that the outflow from IRc2 blows out the material surrounding IRc2 to make the ridge structures, exciting shocked H_2 emission at the surfaces. These H_2 peaks are also considered to be places where the momentum ejected from IRc2 is transferred to the gas surrounding the central source, causing the gas to be blown away.

5.3. *Relation between the H_2 Emission and the Continuum Emission*

Figure 4 shows the H_2 image superposed on the 2.126 μm ($v = +510$ km s^{-1}) continuum image, which was taken right after the on-line frame. The continuum image did not include any line emission except a little H_2 line contamination, which was found to be actually negligible. In Figure 4 the direction of the elongation in the H_2 emission-line contour is close to that for the continuum emission (excluding the bright of self-luminous sources BN and IRc9). Continuum emission was detected on the sides of peaks 1 and 2 that face IRc2, but not on the opposite sides of these peaks. This difference of the spatial distribution between the H_2 line and the 2.126 μm continuum cannot be due to extinction between the Orion-KL region and us.

The polarization images of this region at 2.2 μm obtained by Minchin et al. (1991) and Hough et al. (1986) have shown a centrosymmetric pattern of polarization vectors around IRc2.

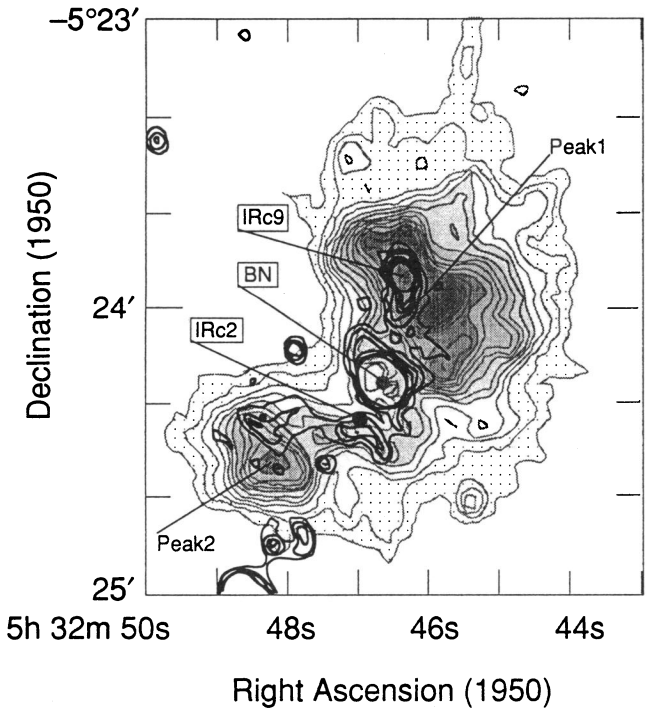

FIG. 4.—H_2 image superposed on the contour of the 2.126 μm ($v = +510$ km s^{-1}) continuum. Contour intervals for the continuum are 1.4×10^{-19} W μm^{-1} cm^{-2} arcsec^{-2} with the lowest contour level 3.3×10^{-19} W μm^{-1} cm^{-2} arcsec^{-2}.

This indicates that the continuum emission around this region is dominated by the reflection of radiation from IRc2, although some vectors indicate BN and IRc9 as possible localized sources of illumination. On the other hand, Hough et al. (1986) and Burton et al. (1991) have obtained the polarization map of H_2 $v = 1$–0 $S(1)$ and found that the polarization vectors are aligned with the outflow axis. They explain this alignment as absorption of H_2 lin emission from the core by aligned grains.

Taking into consideration the difference in the emission mechanisms for the H_2 and the continuum as well as the difference in the spatial distribution, we suggest the following scenario: the outflow from IRc2 blows out and/or destroys the dust to make a cavity, which extends to the positions of peaks 1 and 2. The reflection of the continuum emission from IRc2 will be observed within the extent of the cavity, depending on the properties of scattering (cf. Minchin et al. 1991) and on the extinction of source continuum by the outflow before reflection. On the other hand, H_2 emission will be the strongest at the places where the outflow makes a head-on collision with the dense molecular gas, i.e., peaks 1 and 2. This can make a different distribution between the H_2 and the continuum emission.

6. THE OUTER REGION

In order to show the clumpy distribution of the H_2 emission in the finger region, an unsharp-masking technique was used, i.e., the 7 × 7 pixel median-filtered frame made from Figure 1 was subtracted from Figure 1 itself to emphasize the structure of high spatial frequency. In order to define each clump of the emission with a signal-to-noise ratio optimized for the seeing, we smoothed the unsharp-masked frame taking the running mean by 3 × 3 pixels, which roughly corresponds to the seeing size. We thus set criteria for defining clumps in this resultant frame as follows: (1) any feature having 1 pixel with signal-to-noise ratio exceeding 4, where the noise was measured in the smoothed frame, was defined as a clump, and (2) a feature with more than two peaks which are separated by more than 3 pixels was defined as divided clumps. We tested frames of random noises to find that no clumps or only one clump per frame was artificially produced by using these criteria.

Figure 5 shows the 43 clumps of the H_2 emission identified in the finger region. The positions and intensities of these clumps are given in Table 4. The typical size of a clump in Figure 5 is about a few times 10^3 AU at FWHM when deconvolved for the spatial resolution. The typical mass of hot H_2 molecules for a clump in Figure 5 is of order 10^{-5} $M_\odot$ before correction for extinction.

The positions of the clumps of the H_2 emission are accurate within $\pm 1''$ because all the observed clumps are within a single frame (not in a mosaic of frames). Therefore, it is possible to make an accurate comparison of our data for the 43 clumps with various structures obtained through observations with high spatial resolutions at other wavelengths. In Figure 6*a* we compare our data with the CS (1–0) map obtained by Murata (1991; 5″.6–9″.7 FWHM). The H_2 clumps tend to be located along the filamentary structure identified in the CS (1–0) isocontour, which probably traces the distribution of material. Moreover, the H_2 clumps avoid the peaks of the CS (1–0) intensity. These relations can be more clearly recognized by the comparison with the CS (1–0) velocity-channel maps, with the channel velocities of $v_{LSR} = 1.9$–13.4 km s^{-1} with 0.48 km s^{-1} intervals. The velocity-channel maps show "three-dimensional" CS (1–0) structures, i.e., the velocity structure

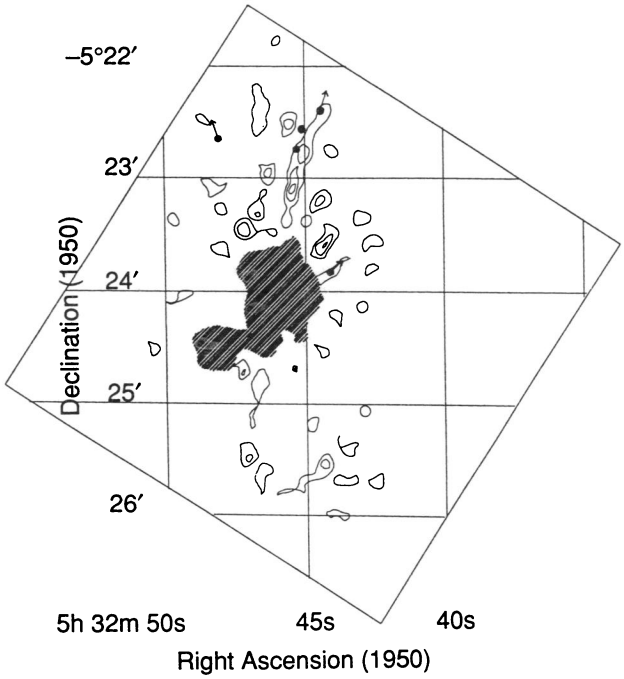

FIG. 5.—Clumps in the H_2 emission defined in the finger region (*contour*). The positions of Herbig-Haro objects are also shown by filled circles with their directions of proper motion (*arrows*; Jones & Walker 1985). The hatched area is the central region, which is discussed separately in § 5.

may resolve the superposition in a line of sight. In order to compare the frame of the H_2 emission with the CS (1–0) velocity-channel maps, we separate the finger region into seven subregions. For each of the subregions, we select a velocity-channel map with the largest intensity within that subregion.

Figure 6*b* shows the comparison of these seven subregions with the velocity-channel maps. The H_2 emission clumps are located along the filamentary structure in CS (1–0), but avoiding the peaks of the CS (1–0) intensity. From this fact we conclude that the H_2 emission originates from the surfaces of the CS (1–0) filaments. This new conclusion implies that the outflow from IRc2 collides with the molecular gas filaments, exciting shocked H_2 emission at the surfaces of the filaments. For several H_2 clumps in the southern part of the frame, the outflow from CS 3/FIR 4, which is the central source of another star-forming region located at 110″ south of IRc2 (Ziurys, Wilson, & Mauersberger 1990; Schmid-Burgk et al. 1990), probably contributes more to the excitation than IRc2.

The hot H_2 column density in the peak of a clump is typically of the order of 10^{18} molecules cm^{-2} from Table 4 and equation (2). When we assume the typical volume density of 10^6 cm^{-3} (Table 6.2 of Murata 1991 implies the density of $\sim 10^6$ cm^{-3} for the region where the CS (1–0) emission was observed), we obtain the typical value of the geometrical thickness of the hot H_2 component, 10^{12} cm (0.07 AU). This is much smaller than the order of the typical clump size, $\sim 10^3$ AU. This fact supports the idea that the H_2 emission from the clumps in the finger region comes from thin sheets at the surfaces of dense matter where the interaction with the outflow from IRc2 occurs.

The positions of Herbig-Haro objects (e.g., Gull et al. 1973; Münch 1977; Axon & Taylor 1984) and their directions of proper motion (Jones & Walker 1985) are shown in Figure 5. From their positions the Herbig-Haro objects seem to be related to the H_2 emission. This kind of relation was suggested by Lane (1989) for one of the Herbig-Haro objects which is located at the northern tip of the strongest H_2 finger-like feature. If the relation between the Herbig-Haro objects and the H_2 emission is real, it implies that the emission mechanism

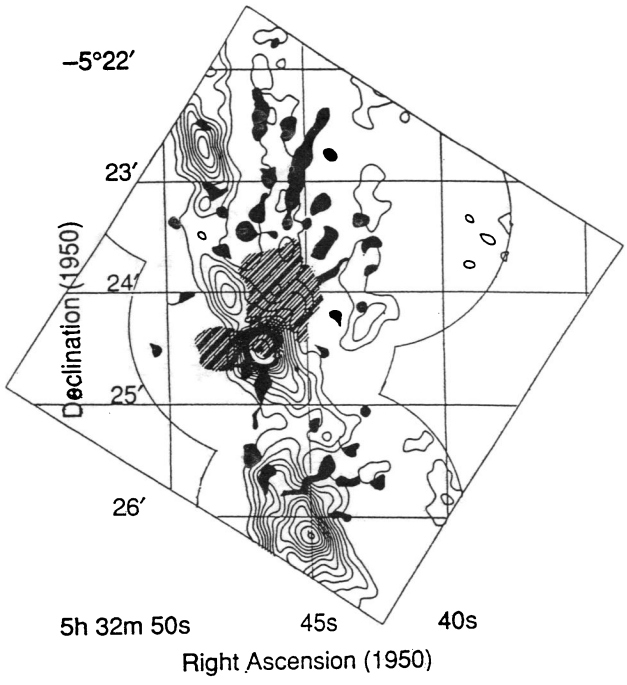

FIG. 6*a*

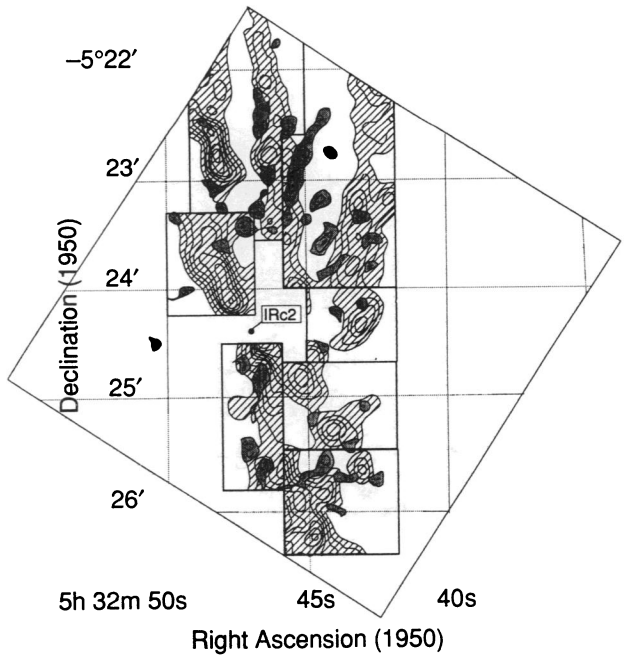

FIG. 6*b*

FIG. 6.—Comparison of the H_2 emission clumps (*gray*) in the finger region with the CS (1–0) map obtained by Murata (1991). (*b*) Comparison with the CS (1–0) velocity-channel maps, shown for seven subregions (see text and Table 4).

TABLE 4

POSITIONS AND INTENSITIES OF H_2 EMISSION CLUMPS IN THE FINGER REGION

NUMBER	POSITION[a] α(1950.0) 5^h32^m+	POSITION[a] δ(1950.0) $-5°+$	INTENSITY[b] ($\times 10^{-22}$ W cm^{-2} arcsec^{-2})	CORRESPONDING CS (1–0) VELOCITY CHANNEL[c] V_{LSR} (km s^{-1})
1.....	42.53	25'43".7	7.7	6.7
2.....	42.57	23 32.4	14.2	7.6
3.....	42.76	23 48.1	14.4	7.6
4.....	42.95	25 03.4	11.4	5.7
5.....	43..04	24 08.5	19.3	6.7
6.....	43.12	23 21.3	12.3	7.6
7.....	43.57	25 25.1	10.6	5.7[d]
8.....	43.84	25 42.3	9.4	6.7[d]
9.....	44.01	24 12.8	28.6	6.7
10.....	44.05	23 49.7	37.4	7.6
11.....	44.07	22 45.9	9.2	...
12.....	44.10	25 58.5	6.7	6.7[d]
13.....	44.35	25 32.3	18.4	6.7[d]
14.....	44.38	22 25.0	5.8	...
15.....	44.43	24 32.2	30.1	6.7
16.....	44.46	23 34.0	50.3	7.6
17.....	44.56	23 53.2	41.7	7.6
18.....	44.57	23 11.9	26.1	...
19.....	44.82	25 11.4	12.3	5.7[d]
20.....	45.00	23 22.3	32.8	7.6
21.....	45.11	22 47.2	30.8	7.6
22.....	45.54	23 05.3	37.2	7.6
23.....	45.64	22 31.3	18.5	8.6
24.....	45.72	23 23.7	42.8	7.6
25.....	46.02	21 45.8	5.9	...
26.....	46.25	23 28.7	46.6	8.6
27.....	46.41	22 57.8	25.4	8.6
28.....	46.47	25 35.8	15.4	8.6[d]
29.....	46.65	22 22.2	16.4	8.6
30.....	46.66	22 31.0	12.5	8.6
31.....	46.67	22 14.1	8.4	8.6
32.....	46.73	24 50.8	36.0	8.6
33.....	46.79	23 19.2	38.8	8.6
34.....	47.08	25 29.1	21.2	8.6[d]
35.....	47.25	24 42.4	53.3	8.6
36.....	47.26	23 27.4	53.0	10.0
37.....	48.06	23 36.9	31.6	10.0
38.....	48.07	23 15.9	21.0	8.6
39.....	48.40	23 05.5	16.2	8.6
40.....	48.69	22 28.8	5.2	8.6
41.....	49.45	24 02.4	21.6	...
42.....	49.73	23 22.4	12.7	10.0
43.....	50.37	24 30.8	21.6	...

[a] The uncertainties, about $\pm 1''$, mainly originate from the pixel scale ($1''.88$ pixel^{-1}).

[b] The intensities were obtained not from the unsharp-masked frame but from the original frame, Fig. 1, although the clumps were defined and discussed by using the unsharp-masked frame. The intensities were obtained by averaging those within 3×3 pixels ($5''.6 \times 5''.6$). The correction for a variation of the transmission over the frame was made assuming that the spatial variation of the peak velocity in Orion-KL was small enough compared with the instrumental resolution and also that the line width in Orion-KL was 50 km s^{-1} (FWHM). The uncertainties of the intensities are larger for clumps with smaller intensities, where the noise is dominated by a readout noise ($1\ \sigma = 1.8 \times 10^{-22}$ W cm^{-2} arcsec^{-2}). Note that the correction for extinction is not carried out. If it is carried out using the *average* extinction value for the central $17'' \times 17''$ region, $A_{2.1\,\mu m} = 2.1$ mag (Davis et al. 1982), these values have to be multiplied by 6.9.

[c] See text.

[d] The H_2 emission clumps, which are considered to be largely affected by the outflow from CS 3/FIR 4.

of the Herbig-Haro objects is similar to the H_2 emission mechanism, i.e., by the interaction between the outflow and the surfaces of the ambient molecular gas.

We show that the H_2 emission from the finger-like features is not reflection but intrinsic, from the comparison with polarization observations by Burton et al. (1991) as well as from discussion of energetics. The region of the H_2 polarization image by Burton et al. (1991) covers 18 clumps of the H_2 emission defined in this section. Figure 1 of Burton et al. (1991) shows a centrosymmetric pattern of vectors for the diffuse component in this region, suggesting an H_2 reflection nebula. This result is consistent with that obtained by Hough et al. (1986). However, a detailed comparison of our image of the clumps with the polarization image by Burton et al. shows that the polarization vectors at the positions of the clumps tend to be smaller and deviate from the centrosymmetric pattern (Fig. 7). Therefore, the H_2 emission from the clumps is thought to be intrinsic, while the diffuse H_2 emission can be reflection. This idea is also

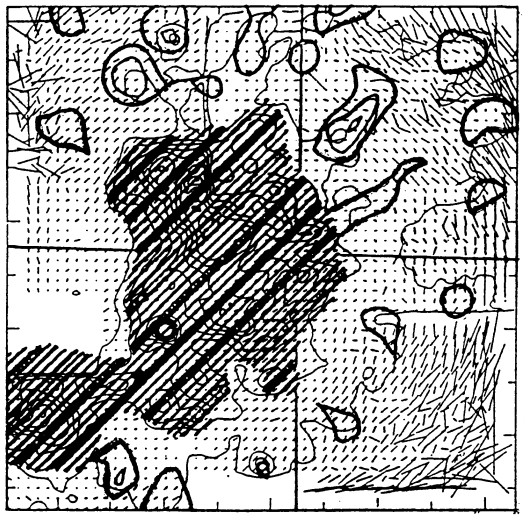

FIG. 7.—Comparison of the H_2 emission clumps (*heavy contour*) with the polarization image by Burton et al. (1991). The scale bar shows a 100% polarized vector. The hatched area is the central region, which is discussed separately in § 5.

supported by a discussion of energetics. The H_2 $v = 1$–0 $S(1)$ luminosity in the finger region is estimated to be $\sim 0.6\ L_\odot$ when not corrected for extinction, which is very similar to that in the central region. If most of the H_2 emission from the finger region were reflection, the efficiency for reflection including the filling factor would have to be as much as ~ 1, which is unlikely for the finger-like features. Moreover, the luminosity in the finger region is underestimated probably by a factor of 3–4 because our resultant frame does not include the diffuse components (cf. Burton & Puxley 1990). The diffuse components include the reflection of the shocked emission from the central region as well as the UV fluorescent component from the Trapezium star cluster. Therefore, it is unlikely from energetics that a significant portion of the H_2 emission of the finger-like features is produced by reflection.

We consider the meaning of the clumpiness in H_2 emission in the finger-like features. The clumpiness is probably not caused by hydrodynamic instabilities in a pressure-confined jet, which were applied by Garden et al. (1990) for interpreting the star-forming regions DR 21 and NGC 2071. Our conclusion that the H_2 emission is radiated at the surfaces of the CS (1–0) molecular filaments implies an external cause for the H_2 clumpiness. There are two possible explanations for the clumpiness of the H_2 emission: (1) If the outflow is uniform, the H_2 clumpiness will tend to correspond to the clumpiness in the CS (1–0) molecular filaments because their surfaces facing to IRc2 will be particularly strongly shocked and the H_2 emission will be radiated there. Some of the H_2 emission clumps may suggest the existence of CS (1–0) clumps even in the case that the CS (1–0) clumps are too small to be resolved. (2) If, on the other hand, the outflow consists of beamlike or bullet-like components in this region, the clumpiness in the H_2 distribution will trace intermittently the path of outflow components because the H_2 emission will be strongly radiated when the outflow components collide with the CS (1–0) molecular filaments. Some components will make an almost head-on collision with a clump in the molecular filaments, and they will stop there or their paths will change slightly. In this case, the H_2 emission will be radiated from surfaces of the filaments facing IRc2. The difference from the case of a uniform outflow is that some CS (1–0) clumps within the extent of the H_2 emission do not have corresponding H_2 emission clumps in the case of beamlike or bullet-like outflow. Although it is difficult to distinguish these two cases from our data, a good correlation of the H_2 emission clumps and the CS (1–0) clumps supports either a uniform outflow or an outflow with beamlike or bullet-like components whose paths have a distance to a neighboring beam or bullet paths comparable to or smaller than the spatial resolution, several arcseconds, in three dimensions. This will give a restriction for the origin for the origin of the outflow and/or the clumpiness of the molecular gas cloud covering peaks 1 and 2, from which some portion of the outflow will escape into the finger region.

We here compare our results with those obtained by Allen & Burton (1993). They imaged the finger region through narrow-band filters, selecting the H_2 $v = 1$–0 $S(1)$ line at 2.122 μm and the [Fe II] $a\ ^4F_{5/2}$–$a\ ^4D_{7/2}$ line at 1.644 μm. They found that [Fe II] emission knots tend to coincide with the tips of hollow structures observed in H_2 emission. From this they argued that individual knots of gas have been ejected into the surrounding molecular cloud. In their interpretation, [Fe II] emission knots are the locations where they strike the dense material, although they did not show the dense material distribution. According to them, H_2 emission is perhaps due to overpressure from the external medium on the cavity created by passage of the knots. From the comparison of our Figure 6*b* and Figure 1 of Allen & Burton (1993), we find that dense material observed in CS (1–0) emission exists at the locations of many [Fe II] knots, including the two brightest ones, which correspond to Herbig-Haro objects. As discussed above, however, our Figure 6*b* shows that H_2 emission is also well correlated with the dense material distribution, clearly, suggesting the importance of the existence of dense material also for the H_2 emission. Although more quantitative comparison among H_2, [Fe II], and CS (1–0) emission for each emission clump might be needed to conclude the dominant emission mechanism, we at least insist on the importance of the interaction with dense material for both the [Fe II] and the H_2 emission.

7. CONCLUSIONS

In the core of the Orion-KL region, we found a curved, bridgelike structure in the H_2 $v = 1$–0 $S(1)$ emission that encroaches on the inner edge of the disk structure observed in CS (1–0) emission. The bridgelike structure cannot be explained by models with an intrinsically collimated flow by twisted magnetic fields, because the structure indicates that the outflow from IRc2 occurs not only toward the bipolar axis but also toward the disk. Channeling by the disk of a more or less isotropic flow from IRc2 into a bipolar flow is a more plausible interpretation. In the outer region, we identify 43 hot H_2 clumps. The H_2 emission from most clumps is radiated at the surfaces of the CS filaments, implying that some components of outflow from IRc2 reach this region to shock the H_2 at those surfaces. The emission mechanism of the Herbig-Haro objects in this region might be similarly due to the interaction between the outflow and the surfaces of molecular filaments, since the HH objects seem to be at least positionally related to the H_2 emission clumps.

We would like to thank Yutaka Uchida, Kazunari Shibata, Masahiko Hayashi, Yasuhiro Murata, Takuya Yamashita, Mamoru Doi, and Shu-ichiro Inutsuka for useful discussion. We thank Masanori Iye, Alan T. Tokunaga, Tetsuo Hasegawa, Hitomi Mikami, Tomofumi Umemoto, Satoshi Yamamoto, and Motohide Tamura for helpful comments. We also acknowledge Masaki Sekiguchi for allowing us to use a program for data reduction. We would like to thank the referees, Dolores Walther and Thomas R. Geballe, for invaluable comments.

REFERENCES

Allen, D. A., & Burton, M. G. 1993, Nature, 363, 54
Aspin, C., Sandell, G., & Walther, D. M. 1992, MNRAS, 258, 684
Axon, D. J., & Taylor, K. 1984, MNRAS, 207, 241
Beckwith, S., Persson, S. E., Neugebauer, G., & Becklin, E. E. 1978, ApJ, 223, 464
Burton, M. G., Minchin, N. R., Hough, J. H., Aspin, C., Axon, D. J., & Bailey, J. A. 1991, ApJ, 375, 611
Burton, M., & Puxley, P. 1990, in The Interstellar Medium in External Galaxies: Summaries of Contributed Papers, ed. D. Hollenbach & H. A. Thronson, Jr. (NASA CP-3084; Washington, DC: NASA), 238
Chernoff, D. F., Hollenbach, D. J., & McKee, C. F. 1982, ApJ, 259, L97
Davis, D. S., Larson, H. P., & Smith, H. A. 1982, ApJ, 259, 166
Downes, D., Genzel, R., Becklin, E. E., & Wynn-Williams, C. G. 1981, ApJ, 244, 869
Garden, R. P., Russell, A. P. G., & Burton, M. G. 1990, ApJ, 354, 232
Geballe, T. R., Persson, S. E., Simon, T., Lonsdale, C. J., & McGregor, P. J. 1986, ApJ, 302, 693
Genzel, R., & Stutzki, J. 1989, ARA&A, 27, 41
Gull, T. R., Goad, L., Chiu, H.-Y., Maran, S. P., & Hobbs, R. 1973, PASP, 85, 526
Hayashi, S. S., Hasegawa, T., Tanaka, M., Hayashi, M., Aspin, C., McLean, I. S., Brand, P. W. J. L., & Gatley, I. 1990, ApJ, 354, 242
Hough, J. H., et al. 1986, MNRAS, 222, 629
Hyland, A. R., Allen, D. A., Barnes, P. J., & Ward, M. J. 1984, MNRAS, 206, 465
Jones, B. F., & Walker, M. F. 1985, AJ, 90, 1320
Khrutskaya, E. V. 1984, Compiled Catalogue of Positions and Proper Motions of 4949 Geodetic Stars from +90° to −90° (Leningrad: Grav. Astron. Obs. Akad. Nauk SSSR)
Lane, A. P. 1989, in ESO Workshop on Low Mass Star Formation and Pre–Main Sequence Objects, ed. B. Reipurth (Garching: ESO), 331
Lee, T. A. 1968, ApJ, 152, 913
Minchin, N. R., et al. 1991, MNRAS, 248, 715
Moran, J. M., Garay, G., Reid, M. J., Wright, M. C. H., & Plambeck, R. L. 1983, ApJ, 271, L31
Münch, G. 1977, ApJ, 212, L77
Murata, Y. 1991, Ph.D. thesis, Univ. Tokyo
Murata, Y., Kawabe, R., Ishiguro, M., Hasegawa, T., Takano, T., Kasuga, T., Morita, K.-I., & Hayashi, M. 1989, in IAU Colloq. 120, Structure and Dynamics of the Interstellar Medium, ed. G. Tenorio-Tagle, M. Moles, & J. Melnick (Heidelberg: Springer-Verlag), 327
Nadeau, D., & Geballe, T. R. 1979, ApJ, 230, L169
Pudritz, R. E., & Norman, C. A. 1983, ApJ, 274, 677
———. 1986, ApJ, 301, 571
Schmid-Burgk, J., Güsten, R., Mauersberger, R., Schulz, A., & Wilson, T. L. 1990, ApJ, 362, L25
Scoville, N. Z., Hall, D. N. B., Kleinmann, S. G., & Ridgway, S. T. 1982, ApJ, 253, 136
Sugai, H., et al. 1994, ApJ, submitted
Taylor, K. N. R., Storey, J. W. V., Sandell, G., Williams, P. M., & Zealey, W. J. 1984, Nature, 311, 236
Turner, J., Kirby-Docken, K., & Dalgarno, A. 1977, ApJS, 35, 381
Uchida, Y., & Shibata, K. 1984, PASJ, 36, 105
———. 1985, PASJ, 37, 515
Wynn-Williams, C. G., Genzel, R., Becklin, E. E., & Downes, D. 1984, ApJ, 281, 172
Ziurys, L. M., Wilson, T. L., & Mauersberger, R. 1990, ApJ, 356, L25